

# Long-Range Wavelike Propagation of Carriers in Methylammonium Lead Iodide Perovskites Thin Films.

Jooyoung Sung<sup>1,2</sup>, Christoph Schnedermann<sup>1,2</sup>, Limeng Ni<sup>1</sup>, Aditya Sadhanala<sup>1,3</sup>, Richard Y.S. Chen<sup>1</sup>, Changsoon Cho<sup>1,4,†</sup>, Lee Priest<sup>2</sup>, Jong Min Lim<sup>2,‡</sup>, Hyun-Kyung Kim<sup>5,1</sup>, Bartomeu Monserrat<sup>1</sup>, Philipp Kukura<sup>2\*</sup>, Akshay Rao<sup>1\*</sup>

## Affiliations:

<sup>1</sup>Cavendish Laboratory, University of Cambridge, J. J. Thomson Avenue, Cambridge CB3 0HE, United Kingdom.

<sup>2</sup>Department of Chemistry, Physical and Theoretical Chemistry Laboratory, University of Oxford, Oxford, United Kingdom.

<sup>3</sup>Clarendon Laboratory, Department of Physics, University of Oxford, Parks Road, Oxford Ox1 3PU, United Kingdom.

<sup>4</sup>School of Electrical Engineering (EE), Korea Advanced Institute of Science and Technology (KAIST), Daejeon, 34141, Republic of Korea.

<sup>5</sup>Department of Materials Science and Metallurgy, University of Cambridge, 27 Charles Babbage Road, Cambridge CB3 0FS, United Kingdom.

<sup>†</sup>Present Address: Dresden Integrated Center for Applied Physics and Photonic Materials, Technische Universität Dresden, 01062 Dresden, Germany

<sup>‡</sup>Present Address: Center for Molecular Spectroscopy and Dynamics, Institute for Basic Science (IBS), Seoul 02841, South Korea

<sup>1</sup>Present Address: Gwangju Bio/Energy R&D Center, Korea Institute of Energy Research (KIER), 270-25 Samso-ro, Buk-gu, Gwangju 61003, Korea.

\*Correspondence to: Akshay Rao ([ar525@cam.ac.uk](mailto:ar525@cam.ac.uk)), Philipp Kukura ([philipp.kukura@chem.ox.ac.uk](mailto:philipp.kukura@chem.ox.ac.uk))

The performance of semiconductor devices is fundamentally governed by charge-carrier dynamics within the active materials<sup>1–6</sup>. While advances have been made towards understanding these dynamics under steady-state conditions, the importance of non-equilibrium phenomena and their effect on device performances remains elusive<sup>7,8</sup>. In fact, the ballistic propagation of carriers is generally considered to not contribute to the mechanism of photovoltaics (PVs) and light emitting diodes (LEDs), as scattering rapidly disrupts such processes after carrier generation via photon absorption or electric injection<sup>9</sup>. Here, we characterise the spatiotemporal dynamics of carriers immediately following photon absorption in organic-inorganic metal-halide perovskite films, using femtosecond transient absorption microscopy (fs-TAM) with 10 fs temporal resolution and 10 nm spatial localisation precision. We find that non-equilibrium carriers propagate ballistically over 150 nm within 20 fs after photon absorption. Our results suggest that in a typical perovskite PV device operating under standard conditions, a large fraction of carriers can reach the charge collection layers ballistically. The ballistic transport distance appears to be limited by energetic disorder within the materials, likely due to disorder-induced scattering. This provides a direct route towards optimisation of the ballistic transport distance via improvements in materials and by minimizing energetic disorder. Our observations reveal an unexplored regime of carrier transport in perovskites, which could have important consequences for device performance.

Organic-inorganic metal-halide perovskites have attracted great attention in recent years due to their remarkable semiconductor properties<sup>10–12</sup>. Despite being solution processed, these materials appear to be largely defect tolerant resulting in long carrier lifetimes and high photoluminescence quantum yields, which facilitate excellent device performance<sup>1–6,13</sup>. The associated charge-carrier transport has been probed under steady-state or quasi steady-state conditions via indirect means such as photoluminescence quenching, indicating carrier diffusion lengths in excess of 1  $\mu\text{m}$  in  $\text{MAPbI}_3$ , the prototypical organic-inorganic metal-halide perovskite system<sup>14,15</sup>. Previous time-resolved microscopy studies resolved the diffusive motion of carriers on ps timescales, but were insensitive to the ultrafast spatial dynamics of non-equilibrium carriers<sup>16,17</sup> due to limited temporal resolution and spatial localization precision (300 fs and 50 nm).

To provide experimental access to the largely unexplored regime of spatiotemporal dynamics occurring on ultrafast timescales usually associated with quantum coherent phenomena<sup>18</sup>, we combined the extreme temporal resolution provided by ultrafast spectroscopy with the nm-level localisation capabilities of high-performance optical microscopes<sup>19</sup>. Delivering a simultaneously near diffraction-limited (264 nm full-width-half-maximum, fwhm, which is equivalent to a standard deviation,  $\sigma$ , of 112 nm) and transform-limited (9.2 fs) pump pulse centred at 580 nm to the sample allows for tight spatiotemporal control of photon absorption (Fig. 1a, Supplementary Sections 1 and 2)<sup>20</sup>. Probing the ensuing carrier dynamics with a counterpropagating and loosely focused (15  $\mu\text{m}$  fwhm,  $\sigma$  of 6.4  $\mu\text{m}$ ) transform-limited (6.8 fs) probe pulse in the near-IR, enables us to simultaneously monitor the spatiotemporal and

spectral dynamics following the initial photoexcitation. We follow the evolution of photoinduced dynamics by comparing the spatial distribution of the carrier population as a function of time, enabling us to quantify carrier motion with a precision far below the diffraction limit (10 nm), limited only by the signal to noise characteristics of the system (Supplementary Sections 3 and 4)<sup>17,21</sup>. Unlike x-ray or electron-based probes, visible light pulses are highly sensitive to a range of electronic dynamics in semiconductor materials. Moreover, by achieving sub-10 fs pulse durations for both pump and probe pulses, we can access the spatially evolving carrier dynamics of both non-, and quasi-equilibrium states<sup>22</sup>.

We focused our investigation on the spatial carrier dynamics of the extremely well characterised methylammonium lead iodide system (MAPI<sub>3-x</sub>Cl<sub>x</sub>)<sup>15,23,24</sup>. To probe the effect of the underlying film morphology on carrier transport at early times, thin films with varying morphology were prepared. These are labelled films **1**, **2** and **3**. Film **1** was prepared using a single-step cold casting method. Film **2** was prepared using single-step hot casting method<sup>25</sup> and film **3** was fabricated in air using a single-step cold casting method in order to fabricate a disordered film. Full details of sample preparation are given in Method Section (Supplementary Fig. 1). The ground-state absorption spectrum of all films exhibits a peak in the wavelength range from 700-760 nm, corresponding to a band-gap energy ( $E_g$ ) of the films (Supplementary Fig. 2)<sup>7</sup>. The early-time dynamics of the films as investigated by conventional transient absorption (TA) spectroscopy (Fig. 1b and Supplementary Figs. 3, and 4) are consistent with previous reports<sup>26-28</sup>. The details of the involved transient species discussed in Supplementary Sections 5. We emphasise two specific observations, which are important for the analysis of the transient microscope results: first, a strong photobleaching band dominates the TA signal between 750 to 760 nm with a broad high energy tail in the 600 to 750 nm range, which is mainly attributed to the phase-space filling effect<sup>29</sup>. Second, early time relaxation dynamics of carriers such as thermalisation and cooling, which generally occur in less than a picosecond, depend strongly on the carrier density. As the carrier density increases, thermalisation accelerates due to the increased carrier-carrier scattering rate, while cooling slows down due to phonon bottleneck effects (Supplementary Figs. 5 and 6)<sup>26-28,30</sup>.

We carried out fs-TAM measurements on film **1** photoexcited at 580 nm (ca. 2.14 eV) at an initial mean carrier density of  $4.28 \times 10^{17} \text{ cm}^{-3}$ , a regime in which the hot phonon effect is negligible<sup>30</sup>. The high energy side of the photobleaching band of the semiconductor is not only directly correlated with the electron and hole Fermi distribution, but also with the spectral features stemming from non-thermalised carriers<sup>26</sup>. As depicted in the schematic diagram of the energy dispersion relation in  $k$ -space (Fig. 1c), initially generated carriers assume a non-equilibrium distribution around the pump energy<sup>31</sup>. Concomitant phase space and band filling effects lead to a strong photobleaching band and a broad high energy tail<sup>29</sup>. The non-equilibrium carriers then undergo carrier-carrier scattering within tens of fs and their energy is redistributed to form a quasi-equilibrium carrier distribution, with enhanced and broad spectra near  $E_g$ . This population will subsequently cool to reach a thermal equilibrium with the lattice over hundreds of fs. Consequently, by monitoring carriers generated around the pump energy

or at the high energy side of the photobleaching band, we can explore the spatial transport dynamics of non-equilibrium carriers.

Fig. 1d shows the fs-TAM images obtained from film **1**, probing the high-energy tail of the photobleaching band (ca. 720 nm), i.e. the non-equilibrium carrier distribution. We note that fs-TAM images of each film were obtained by averaging the images taken over 50 runs on at least five different spots across multiple films, to eliminate artefacts from spot-to-spot variations in the sample. The x-y axis in Fig. 1d plots the spatial position and the z axis (in false colour) gives the signal strength at each spatial position. Each image provides the spatial profile of the carrier distribution. Intriguingly, the fs-TAM images recorded as a function of time clearly reveal a pronounced spatial expansion of the carrier distribution within a few tens of fs. This implies that carriers are moving rapidly at the earliest times after photoexcitation.

In order to quantify the spatiotemporal evolution, we fitted the fs-TAM images with an isotropic 2D Gaussian function (Supplementary Section 3) and extracted the corresponding standard deviation,  $\sigma$ , as shown in Fig. 1e (see also Supplementary Figs. 7-10)<sup>17</sup>. At zero-time delay the fs-TAM signal is expected to be spatially distributed only within the pump area. Consistent with this we find that the width of the fs-TAM signal obtained at near-zero pump-probe delay,  $\sigma(0)$ , is close to the diffraction limit of our microscope ( $166 \pm 10$  nm vs. 129 nm for a diffraction limited spot, Supplementary Fig. 11 and Table 1), representing the initial carrier distribution. Shortly after photoexcitation, a rapid expansion of the carrier distribution occurs, which we quantify by calculation of the mean-squared displacement ( $\text{MSD} = \sigma^2(t) - \sigma^2(0)$ ) as plotted in Fig. 2a (black line). We find that the MSD of the non-equilibrium carriers in film **1** grows non-linearly, in contrast to the linear behaviour expected for normal diffusion. Furthermore, the MSD within the first 20 fs is well described by a power law fit,  $\sigma^2(t) - \sigma^2(0) = Dt^\alpha$ , giving an  $\alpha$  value of  $2.00 \pm 0.30$  (where  $D$  is the diffusion coefficient).  $\alpha = 2$  signifies that the non-equilibrium carriers in film **1** propagate in a ballistic manner during the initial 20 fs after photoexcitation. In Figure 2b we plot the relative change in the width of the carrier distribution according to  $l(t) \sim \sqrt{\sigma^2(t) - \sigma^2(0)}$  as a function of time. The linear region in this plot, shown via the fits, gives the ballistic carrier transport length. For film **1**, this value is measured to be  $l = 153 \pm 6$  nm, a remarkably large distance. No comparable ultrafast microscopy measurements have been performed for other semiconductor systems, but electrical measurements in GaAs transistors suggest a ballistic transport lengths of 85 nm<sup>32</sup>.

To investigate the effect of film morphology on the ballistic transport dynamics of the non-equilibrium carriers, we conducted fs-TAM measurements on films **2** and **3** (fabrication, see in Method Section). The SEM images for all thin films exhibited polygon grains with film **1** and **3** exhibiting large voids in the vicinity of grains as shown in Figs. 3d-e and Supplementary Fig. 1. We emphasize that in all films the grain size (ca., 2, 20 and 1  $\mu\text{m}$  for film **1**, **2**, and **3**, respectively) is at least two times larger than the pump spot size used in fs-TAM, thus providing

quasi-single crystalline condition for our measurements (Supplementary Figs. 1 and 12). These grain sizes are also typical of perovskite films used in high performance devices.

As shown in Fig. 2a (red and blue lines), similar to film 1, the MSD traces for film 2 and 3 are well described by a power law fit at very early times (up to 15 fs). The obtained  $\alpha$  values of  $\sim 2$  ( $2.04 \pm 0.12$ , and  $2.30 \pm 0.04$  for film 2 and 3, respectively) match those obtained for films 1 and provide strong evidence that the ballistic transport of non-equilibrium carriers is universal in  $\text{MAPI}_{3-x}\text{Cl}_x$  thin films in spite of different film fabrication protocols and morphology. However, despite having similar  $\alpha$  values, the expansion obtained for film 2 and 3 is significantly reduced and stops slightly earlier at  $\sim 15$  fs. As shown in Fig. 2b, the ballistic transport lengths of film 2 and 3 were determined to be  $52 \pm 5$  and  $68 \pm 6$  nm, respectively, much shorter than that of film 1. This suggests that while all films support ballistic transport at early times, the magnitude is controlled by film morphology.

The ballistic transport of carriers in semiconductors is known to be sensitive to energetic disorder<sup>33,34</sup>. To assess the role of disorder, here we performed photoluminescence microscopy measurements, which provide a sensitive probe of spatial disorder in the films. In Fig. 3a-c and Supplementary Fig. 13, we compare the wide-field photoluminescence intensity images of films 1, 2 and 3 recorded at 760 (left panel) and 790 nm (right panel). Any spatial energetic disorder in the films is reflected in its photoluminescence spectrum and hence leads to different spatial distributions of photoluminescence intensity between the two wavelengths. Whereas the photoluminescence intensity images of film 1 exhibit similar spatial distributions at 760 and 790 nm, films 2 and 3 exhibit different spatial distributions. This observation indicates that film 2 and 3 contain a large spatial energetic disorder than film 1. To quantify the underlying disorder, we computed the photoluminescence intensity ratio  $r_x = (I_{x, 760\text{nm}} + 1)/(I_{x, 790\text{nm}} + 1)$ , where  $x$  is position for each films and produced corresponding histograms from the spatial maps as shown in Fig. 3d-f and Supplementary Fig. 13. The histograms of film 1 displays a tight distribution with a standard deviation of 0.056. By contrast, the histograms of film 2 and 3 exhibit a much broader distribution with standard deviations of 0.081 and 0.075, respectively. These measurements are indicative of spatial energetic disorder in the films which increases in the order of  $1 < 3 < 2$ . Since the ballistic transport length decreases in the same order (Supplementary Fig. 14), we propose that the energetic disorder limits the ballistic transport length of the non-equilibrium carriers in perovskite thin films.

To elucidate the effect of carrier density on the ballistic transport dynamics of the non-equilibrium carriers, we performed fs-TAM measurements as a function of pump fluence with the initial mean carrier density ranging from  $5.40 \times 10^{17}$  to  $2.50 \times 10^{18} \text{ cm}^{-3}$  (Supplementary Figs. 15-17). We compare film 1, Fig 4a, which showed the lowest energetic disorder and longest ballistic transport length, with film 2, Fig 4b, which exhibited the highest energetic disorder and shortest ballistic transport length. For film 1 we find that as the mean carrier density increases from  $5.40 \times 10^{17}$  to  $2.50 \times 10^{18} \text{ cm}^{-3}$ , the corresponding ballistic transport length

reduces from  $153 \pm 6$  to  $66 \pm 10$  nm (Fig. 4a and c). This suggests that in this sample at higher carrier densities carrier-carrier scattering is the dominant process limiting ballistic transport. When disorder is sufficiently low the non-equilibrium carriers have more time to move ballistically and travel further before they scatter with other carriers. As the carrier density increases, the motion of the non-equilibrium carriers becomes more confined, leading to a reduced transport length. We note that while at high fluence there is a saturation behavior of the  $\Delta T/T$  signal, at the lower fluences where we measure the large ballistic transport lengths the  $\Delta T/T$  signal scales linearly with pump fluence, indicating the lack of non-linear effects on the expansion (Supplementary Section 6).

In sharp contrast, for film **2** there is no noticeable difference in the ballistic transport length ( $52 \pm 11$ ,  $49 \pm 11$ , and  $49 \pm 10$  nm Fig. 4b and c) with change in carrier density. This suggests that in a highly energetically disordered film (such as film **2**, Fig. 3b) the ballistic transport breaks down before carriers have a chance to scatter off each other and it is the spatial energetic disorder that limits transport. We furthermore find for film **1** that the ballistic transport length for carrier densities below  $1.28 \times 10^{18} \text{ cm}^{-3}$  exhibit almost identical values (Fig. 4c, grey curve) despite a difference in the initial carrier density of a factor of 3. This observation indicates that below a certain carrier density threshold carrier-carrier scattering no longer governs the ballistic transport distance and instead energetic disorder takes over.

The mean carrier transport velocity of  $5.0 \times 10^6 \text{ ms}^{-1}$  extracted from the time-evolution profiles of ballistic transport length ( $7.6 \times 10^6$ ,  $4.4 \times 10^6$  and  $2.9 \times 10^6 \text{ ms}^{-1}$  for film **1**, **2**, and **3**, respectively as shown in Fig. 2b) is in approximate agreement with the group velocity of electrons within the conduction band as modelled by density functional theory (DFT) in conjunction with the HSE exchange-correlation functional (approaching  $1.0 \times 10^6 \text{ ms}^{-1}$ , Supplementary Fig. 18, see Supplementary Section 7 for details of calculations). This implies that photogenerated carriers propagate as the group velocity (Fig. 1c) and have a non-interacting nature at least at the earliest times following photon absorption<sup>29</sup>. This also helps rationalise our observations on the relationship between energetic disorder and ballistic transport lengths, as the disordered regions would act as scattering sites whose effect is to halt the ballistic propagation. Future theoretical and experimental work will be needed to identify the exact details of the disorder induced scattering processes, but it is evident from the results presented here that energetic disorder plays a large role in the process and reducing spatial energetic disorder is a clear route to increasing ballistic transport lengths.

We stress that our observation of ballistic transport relates only to non-equilibrium carriers, before scattering disrupts their propagation on a timescale of tens of femtoseconds. Once this ballistic propagation breaks down, we observe no further rapid transport of quasi-equilibrium hot-carriers up to 5 ps (Supplementary Fig. 8, see also Supplementary Sections 8 and 9 for the details). Consequently, hot carriers do not play a significant role in the operating mechanism of PV devices under normal conditions. In contrast, the non-equilibrium carriers studied here

could play a role, as ballistic transport operates under low excitation densities relevant to working PV devices. The continuous nature of solar illumination (AM 1.5G) leads to carrier densities of  $10^{14}$ - $10^{15}$  cm<sup>-3</sup> for perovskite PV devices due to their long carrier lifetime of several hundreds of nanoseconds resulting in a carrier density two orders of magnitude lower than those studied here implying significantly reduced carrier-carrier scattering<sup>31</sup>. Furthermore, unlike for pulsed excitation, solar illumination continuously produces carriers and a majority of carriers at any time are part of the cold population, for which the scattering cross-section will be reduced. Thus, in a working device under solar illumination, carriers can move at the group velocity, i.e. ballistically, immediately after photogeneration until scattered by other carriers or localised by disorder within the film. Based on the measurements here, carriers are able to propagate with a ballistic transport distance of at least 150 nm under operational device conditions.

In order to understand the possible effect on ballistic transport on the performance on a working perovskite device we constructed a full optical model for a device using the transfer matrix formalism, taking into account electrodes, charge transport layers and an active layer of variable thickness (see Supplementary Section 10 for full details of the model). We use a ballistic transport distance of 150 nm, which is the value measured in film **1**. Fig. 4d plots the ballistic charge collection efficiency, i.e. the fraction of carries that reach the charge collection layers ballistically, as a function of the thickness of the perovskite film. Values are shown for collection at both the front and back charge transport layer and also the sum. For very thin films a large fraction of the carriers can reach the charge collection layer ballistically, whereas for films of thickness 400-600 nm, which are typical for PV devices, 25% of carriers can reach the charge collection layer ballistically. This value effectively saturates due to the absorption profile of light within the device, with a large fraction of light absorbed towards the front of the device (see Supplementary Section 10 for details). While transport to the charge collection layer is separate from charge injection in these layers, these results suggest that ballistic transport could play a significant part role in devices. It is possible that future charge collection and injection contacts could be engineered to harness these effects for a range of device applications.

Our results demonstrate that non-equilibrium carriers can propagate ballistically over distances of 150 nm in perovskite thin films. Such ballistic motion has to date not been considered to be of relevance in PV operation and our results call for a re-evaluation of current device models. Moreover, future materials and devices can be engineered to efficiently harness the phenomena to create improved and novel functionalities. Our experimental methodology also shows that the longstanding challenges of simultaneously achieving high temporal resolution and high spatial localisation precision are surmountable and pave the way towards nanoscale-sensitive characterization of optically-induced electronic processes on the femtosecond timescale.

## Method:

**Sample preparation:** All materials were purchased from Sigma-Aldrich or Dysol and were used as received. A mixture of  $\text{PbCl}_2$  and  $\text{CH}_3\text{NH}_3\text{I}$  (MAI) in a 1:3 molar stoichiometric ratio were prepared in N,N-dimethylformamide solvent by constant stirring until dissolved. Film **1** was prepared by using the cold-casting method, which the solution was spin-coated on top of clean glass substrates at 2000 rpm for 60 seconds and annealed at 100 °C for 5 min to form thin films. Film **2** was prepared by the hot-casting method. A hot (~70°C) solution was casted onto a substrate maintained at a temperature of upto 180 °C and subsequently spin-coated (15s). Finally, it is annealed at 100°C to obtain a uniform film. Both film **1** and **2** were fabricated and encapsulated inside a nitrogen filled glove box. On the other hand, under the air atmosphere, Film **3** was fabricated by using the cold-casting method as described above.

**Femtosecond transient absorption spectroscopy (fs-TA):** The ultrafast (15 fs time resolution) TA experiments were performed using a Yb:KGW based amplified system (Light Conversion, Pharos) providing 14.5 W at 1030 nm and 38 kHz repetition rate. The probe beam is generated by focusing a portion of the fundamental in a 4 mm YAG crystal to generate a white light continuum (WLC). The pump beam is generated using a non-collinear optical parametric amplifier (NOPA). The WLC generated from the 3 mm YAG crystal is focused onto the nonlinear crystal (37° cut BBO, type I, 5° external angle) and are pumped by the third harmonic of the fundamental (Light Conversion, HIRO). The NOPA output consists of 600  $\mu\text{W}$  pump pulses at the centre wavelength of 525 nm and spectral bandwidth of 25 nm. The pump pulses are then compressed using a pair of chirped mirrors. The 525 nm NOPA pump pulses and WLC probe beam are overlapped in the sample with a 8.7° angle. The WLC probe beam is delayed using a computer-controlled piezoelectric translation stage. A sequence of probe pulses with and without pump is generated using a chopper wheel on the pump beam. After the sample, the probe pulses are seeded through a monochromator and using a silicon line scan camera (AViiVA EM2/EM4) so as to measure the transient difference absorption between 540 and 1000 nm at a 19 kHz rate.

**Femtosecond transient absorption microscopy (fs-TAM):** A Yb:KGW laser system (Pharos, Light Conversion) provided 200 fs, 30  $\mu\text{J}$  pulses at 1030 nm with 200 kHz repetition rate. The output beam was divided by a beam splitter and seeded two broadband WLC stages. The probe WLC was generated in a 3 mm YAG crystal and adjusted to cover the wavelength range from 650-950 nm by a fused-silica prism-based spectral filter. In contrast, the pump WLC was generated in a 3 mm sapphire crystal to extend the WLC to 500 nm, and short-pass filtered at 650 nm (Thorlabs, FESH650). A set of chirped mirrors (pump; 109811, Layertec, probe; DCM9, Venteon) and a pair of fused silica wedges (Layertec) compressed the pulses to 9.2 fs (pump) and 6.8fs (probe), as verified by second-harmonic generation frequency-resolved optical gating (SHG-FROG) (Supplementary Section 2). In addition, the pump pulse was pre-compressed with another set of chirped mirrors (109811, Layertec) to account for dispersion



in the microscope optics. The corresponding cross-correlation curve simulated with the retrieved pump and probe temporal profiles given in Supplementary Section 2 shows an effective time resolution of 13 fs. A mechanical translation stage (Newport, CONEX-AG-LS25-27P) was used to delay the probe with respect to the pump. A clean TEM<sub>00</sub> mode for pump was achieved with a pinhole. The pump was collimated to completely fill the aperture of objective lens and was focused onto the sample by a 1.2 NA oil immersion objective (100x) to the near diffraction limited spot (ca. 270 nm (fwhm)) while the probe pulse was delivered into the sample with the relatively large focal spot (ca. 15  $\mu$ m) from the opposite direction. The transmitted probe pulse was collected by the same objective and sent to an EMCCD camera (QImaging, Rolera<sup>TM</sup> Thunder). The total magnification of the imaging system was 288x. The scattered pump light was rejected by a 650 nm long-pass filter (Thorlabs, FEL650) inserted in front of the camera. Differential imaging was achieved by modulating the pump beam at 30 Hz by a mechanical chopper. Moreover, fs-TAM images were obtained by averaging images taken over 50 runs at ten different spots for low pump fluence measurements and at five different spots for relatively high fluence measurement for each samples.

### Data availability

The data underlying all figures in the main text and supplementary information are publicly available at <https://doi.org/xxxxxxx>.

### References and Notes:

1. Tan, Z. *et al.* Bright light-emitting diodes based on organometal halide perovskite. *Nat. Nanotechnol.* **9**, 687–692 (2014).
2. Burschka, J. *et al.* Sequential deposition as a route to high-performance perovskite-sensitized solar cells. *Nature* **499**, 316–319 (2013).
3. Senanayak, S. P. *et al.* Understanding charge transport in lead iodide perovskite thin-film field-effect transistors. *Sci. Adv.* 1–11 (2017).
4. Lee, M. M., Teuscher, J., Miyasaka, T., Murakami, T. N. & Snaith, H. J. Efficient hybrid solar cells based on meso-superstructured organometal halide perovskites. *Science* **338**, 643–648 (2012).
5. Chin, X. Y., Cortecchia, D., Yin, J., Bruno, A. & Soci, C. Lead iodide perovskite light-emitting field-effect transistor. *Nat. Commun.* **6**, 1–9 (2015).
6. Xing, G. *et al.* Low-temperature solution-processed wavelength-tunable perovskites for lasing. *Nat. Mater.* **13**, 476–480 (2014).
7. Herz, L. M. Charge-carrier dynamics in organic-inorganic metal halide perovskites. *Annu. Rev. Phys. Chem.* **67**, 65–89 (2016).
8. Ulbricht, R., Hendry, E., Shan, J., Heinz, T. F. & Bonn, M. Carrier dynamics in semiconductors studied with time-resolved terahertz spectroscopy. *Rev. Mod. Phys.* **83**, 543–586 (2011).
9. Shah, J. *Ultrafast Spectroscopy of Semiconductors and Semiconductor Nanostructures*. **7**, (Springer, 2006).

10. Li, W. *et al.* Chemically diverse and multifunctional hybrid organic-inorganic perovskites. *Nat. Rev. Mater.* **2**, 1–18 (2017).
11. Brenner, T. M., Egger, D. A., Kronik, L., Hodes, G. & Cahen, D. Hybrid organic - Inorganic perovskites: Low-cost semiconductors with intriguing charge-transport properties. *Nat. Rev. Mater.* **1**, 1–16 (2016).
12. Huang, J., Yuan, Y., Shao, Y. & Yan, Y. Understanding the physical properties of hybrid perovskites for photovoltaic applications. *Nat. Rev. Mater.* **2**, 1–19 (2017).
13. García De Arquer, F. P., Armin, A., Meredith, P. & Sargent, E. H. Solution-processed semiconductors for next-generation photodetectors. *Nat. Rev. Mater.* **2**, 1–15 (2017).
14. Stranks, S. D. *et al.* Electron-hole diffusion lengths exceeding 1micrometer in an organometal trihalide perovskite absorber. *Science* **342**, 341–344 (2013).
15. Xing, G. *et al.* Long-range balanced electron- and hole-transport lengths in organic-inorganic CH<sub>3</sub>NH<sub>3</sub>PbI<sub>3</sub>. *Science* **342**, 344–347 (2013).
16. Guo, Z. *et al.* Long-range hot-carrier transport in hybrid perovskites visualized by ultrafast microscopy. *Science* **62**, 59–62 (2017).
17. Guo, Z., Manser, J. S., Wan, Y., Kamat, P. V. & Huang, L. Spatial and temporal imaging of long-range charge transport in perovskite thin films by ultrafast microscopy. *Nat. Commun.* **6**, 1–8 (2015).
18. Brédas, J. L., Sargent, E. H. & Scholes, G. D. Photovoltaic concepts inspired by coherence effects in photosynthetic systems. *Nat. Mater.* **16**, 35–44 (2016).
19. Von Diezmann, A., Shechtman, Y. & Moerner, W. E. Three-dimensional localization of single molecules for super-resolution imaging and single-particle tracking. *Chem. Rev.* **117**, 7244–7275 (2017).
20. Schnedermann, C. *et al.* Ultrafast tracking of exciton and charge carrier transport in optoelectronic materials on the nanometer scale.  
<https://pubs.acs.org/doi/pdf/10.1021/acs.jpcclett.9b02437> (2019)
21. Nah, S. *et al.* Ultrafast imaging of carrier cooling in metal halide perovskite thin films. *Nano Lett.* **18**, 1044–1048 (2018).
22. Schnedermann, C. *et al.* Sub-10 fs time-resolved vibronic optical microscopy. *J. Phys. Chem. Lett.* **7**, 4854–4859 (2016).
23. Richter, J. M. *et al.* Ultrafast carrier thermalization in lead iodide perovskite probed with two-dimensional electronic spectroscopy. *Nat. Commun.* **8**, 1–7 (2017).
24. Jha, A. *et al.* Direct observation of ultrafast exciton dissociation in lead iodide perovskite by 2D electronic spectroscopy. *ACS Photonics* **5**, 852–860 (2018).
25. Zhao, B. *et al.* High open-circuit voltages in tin-rich low-bandgap perovskite-based planar heterojunction photovoltaics. *Adv. Mater.* **29**, (2017).
26. Price, M. B. *et al.* Hot-carrier cooling and photoinduced refractive index changes in organic-inorganic lead halide perovskites. *Nat. Commun.* **6**, 1–8 (2015).
27. Manser, J. S. & Kamat, P. V. Band filling with free charge carriers in organometal halide perovskites. *Nat. Photonics* **8**, 737–743 (2014).
28. Yang, Y. *et al.* Observation of a hot-phonon bottleneck in lead-iodide perovskites. *Nat. Photonics* **10**, 53–59 (2016).

29. Hunsche, S., Leo, K., Kurz, H. & Kohler, K. Exciton absorption saturation by phase-space filling: influence of carrier temperature and density. *Phys. Rev. B* **49**, 16565–16568 (1994).
30. Fu, J. *et al.* Hot carrier cooling mechanisms in halide perovskites. *Nat. Commun.* **8**, 1–9 (2017).
31. Richter, J. M. *et al.* Ultrafast carrier thermalization in lead iodide perovskite probed with two-dimensional electronic spectroscopy. *Nat. Commun.* **8**, 1–7 (2017).
32. Hayes, R. Dynamics of extreme nonequilibrium electron transport in GaAs. *IEEE J. Quantum Electron.* **22**, 1744–1752 (1986).
33. Beenakker, C.W.J., Houten, H. van. Quantum transport in semiconductor nanostructures. *Solid State Phys.* **44**, 1–228 (1991).
34. Zhang, W. *et al.* Enhanced optoelectronic quality of perovskite thin films with hypophosphorous acid for planar heterojunction solar cells. *Nat. Commun.* **6**, 1–9 (2015).

**Acknowledgments:** We thank the Engineering and Physical Sciences Research Council (EPSRC) and the Winton Programme for the Physics of Sustainability for funding. This project has received funding from the European Research Council (ERC), under the European Union’s Horizon 2020 research and innovation program (grant agreement No 758826). J. S. acknowledges financial support from the Basic Science Research Program through the National Research Foundation of Korea (NRF) funded by the Ministry of Education (2016R1A6A3A03009054). L.N. acknowledges support from the Jardine Foundation. C.S. acknowledges financial support from the Royal Commission for the Exhibition of 1851. A.S. acknowledges support from the UKRI Global Challenge Research Fund project, SUNRISE (EP/P032591/1), UKIERI project for the Physics of Sustainability (University of Cambridge) and Indo-UK joint project-APEX Phase-II.

**Contributions:** C.S., J.S., J.M built the fs-TAM setup. J.S. carried out TAM measurements with L.P. J.S. analysed the data. L.N. and A.S. fabricated and performed steady-state characterisation of the MAPI thin films. H.-K.K. performed SEM measurement. R.C. and C.C. developed the charge collection model. B.M. performed the band structure calculations. J.S, P.K. and A.R wrote the paper. P.K. and A.R supervised the work.

**Competing interests:** The authors declare no competing financial interests.

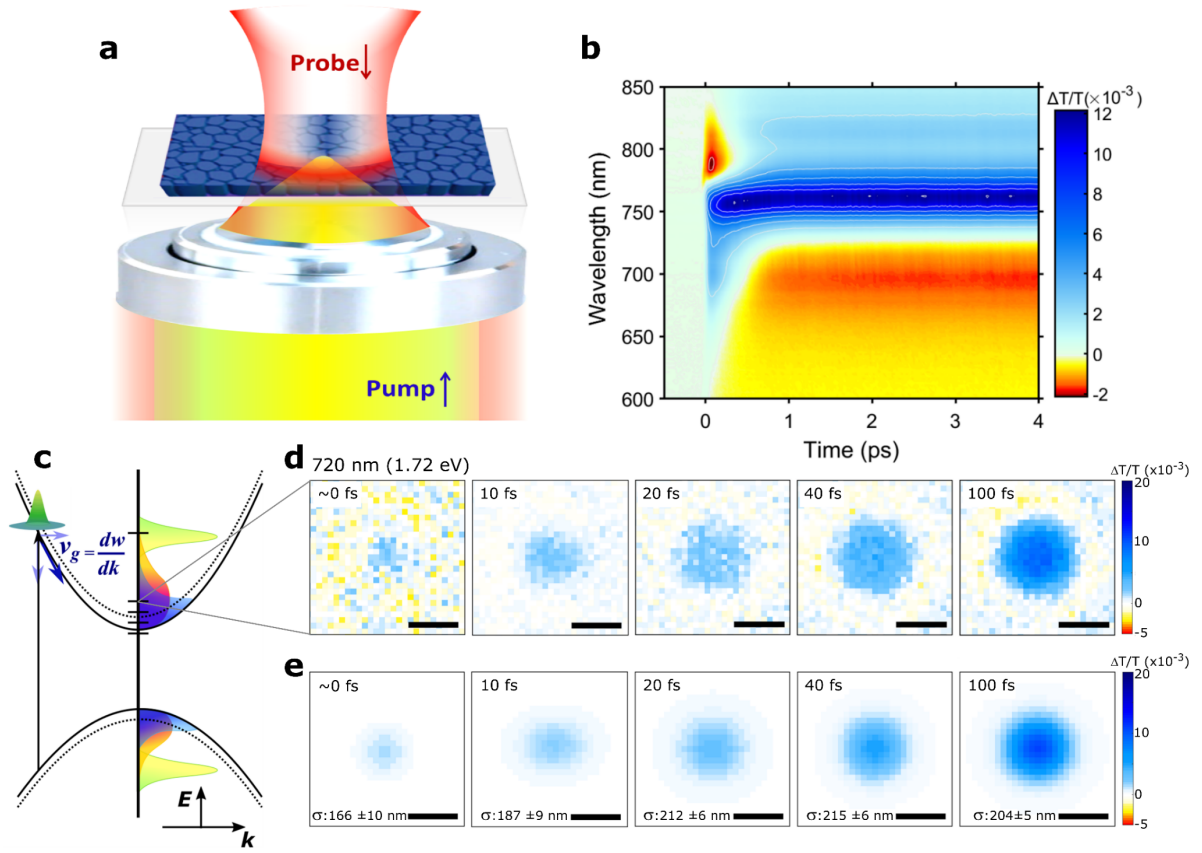


**Figure 1. Representative transient absorption spectroscopy and microscopy results of  $\text{MAPI}_{3-x}\text{Cl}_x$  thin film.** **a**, Schematic of fs-TAM. A near diffraction-limited (264 nm full-width-half-maximum, fwhm) and transform-limited (9.2 fs, 580 nm) pump pulse is delivered to the sample with a counterpropagating and loosely focused (15  $\mu\text{m}$  fwhm)  $<6.8$  fs probe pulse. Comparison of snapshots of the spatial distribution of the carrier population enabling us to measure carrier motion with a precision (10 nm) far below the diffraction limit, limited only by the signal to noise of the system **b**, A two-dimensional transient differential transmission map at an initial carrier density of  $1.28 \times 10^{17} \text{ cm}^{-3}$ . **c**, Schematic diagram of carrier dynamics at early times: initial photon absorption leads to the formation of a non-equilibrium carrier population at the pump energy (green-blue shaded region), carrier-carrier scattering then leads to thermalisation and the formation of a quasi-equilibrium ‘hot-carrier’ population on sub-100 fs timescales (yellow-red shaded region), the hot-carriers then cool to the lattice temperature (blue-purple shaded region). At the earliest times carriers can propagate as wavepackets at the group velocity (green shaded wavepacket) **d**, Representative fs-TAM images as a function of pump probe delay at the high energy side (720 nm). A spectral bandwidth of 10 nm is determined by inserting adequate band-pass filters in the imaging path. Signal intensity of fs-TAM images at zero and 10 fs pump-probe delay was scaled by a factor of 5 and 2, respectively for clarity. **e**, The corresponding carrier distribution functions fitted with an isotropic 2D Gaussian functions. The inserted  $\sigma$  values represent the extracted width of carrier distribution at each pump-probe delay. Scale bars, 500 nm.

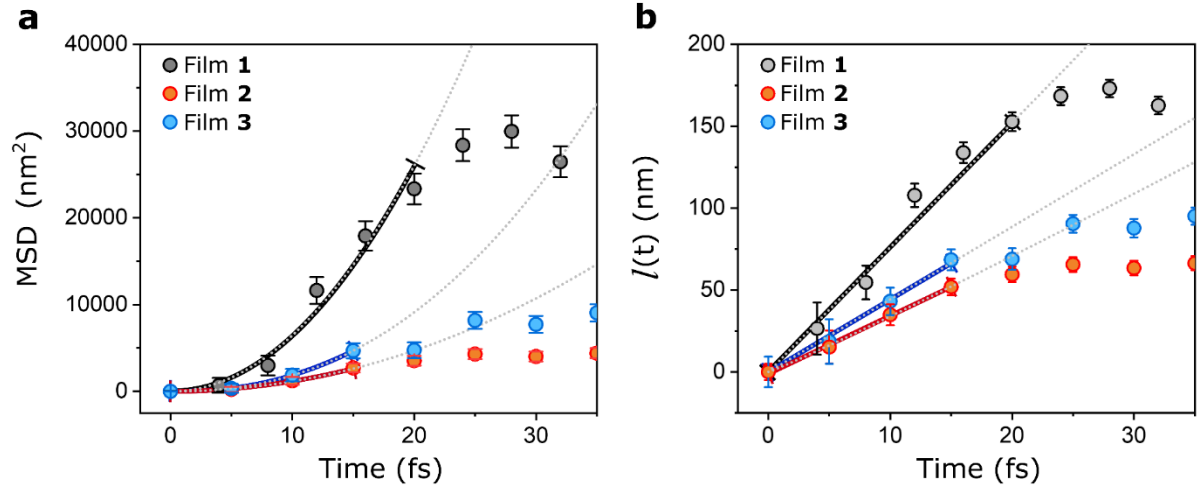


**Figure 2. Spatial dynamics of non-equilibrium carriers.** **a**, Time evolution of the mean-squared displacement (MSD) profile,  $\text{MSD} = \sigma^2(t) - \sigma^2(0)$ , where  $\sigma^2(0)$  is the standard deviation of the spatial carrier distribution obtained at zero pump-probe delay. The grey dotted lines represent fits using the power law equation,  $Dt^a$ , where  $D$  is the diffusion coefficient. The color lines indicate the region of the best fit. **b**, Time evolution of relative changes in the width of the carrier distribution,  $\sigma(t)$ , which is interchangeable with ballistic transport length,  $l(t) \approx \sqrt{\sigma^2(t) - \sigma^2(0)}$  in the ballistic transport region. The grey dotted line represents the resultant fit of  $l \approx vt$ , where  $v$  is a coefficient which provides the velocity of ballistic transport. The color lines represent the region of the best fit. **Error bars represent standard deviation widths from the 2D Gaussian fit as discussed in detail in Supplementary Section 4.**

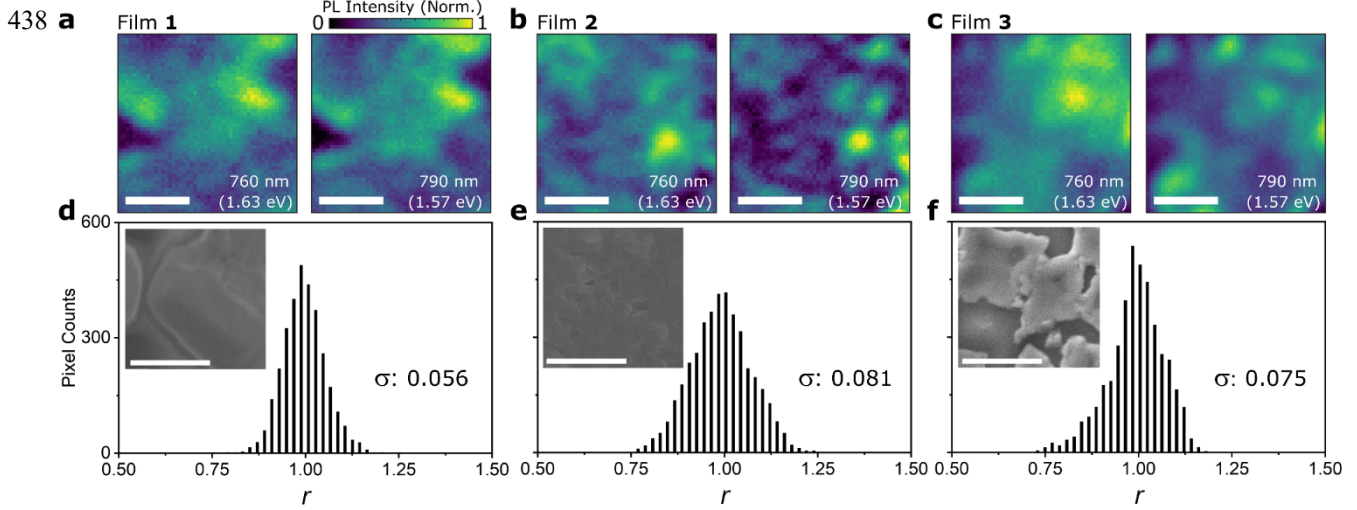


**Figure 3. Photoluminescence (PL) behavior of three different perovskite thin films.** **a**, **b**, and **c**, The wide-field PL images recorded at 760 nm (1.63 eV) (left) and 790 nm (1.57 eV) (right) of film **1**, **2**, and **3**, respectively. Here, we only plot representative images obtained at the spot ‘A’ for each  $\text{MAPI}_{3-x}\text{Cl}_x$  thin films. Additional PL images recorded at two additional spots (B and C) are shown in Supplementary Fig.13. **d**, **e**, and **f**, The histograms of the PL intensity ratio of film **1**, **2**, and **3**, respectively. The histograms were obtained as follows: First, the PL intensity images were normalized to 1. Second, we calculated the PL intensity ratio between the two probing wavelength by following equation;  $r_x \approx \frac{I_{x,760\text{nm}} + 1}{I_{x,790\text{nm}} + 1}$ . Finally, the histogram, which provides a visual representation of the PL intensity ratio distribution, was created. The inset ‘ $\sigma$ ’ values represent the standard deviation of each histograms, provide an estimate of energetic disorder. Inset images reveal the representative SEM images for film **1**, **2**, and **3**. Scale bars, 500 nm.

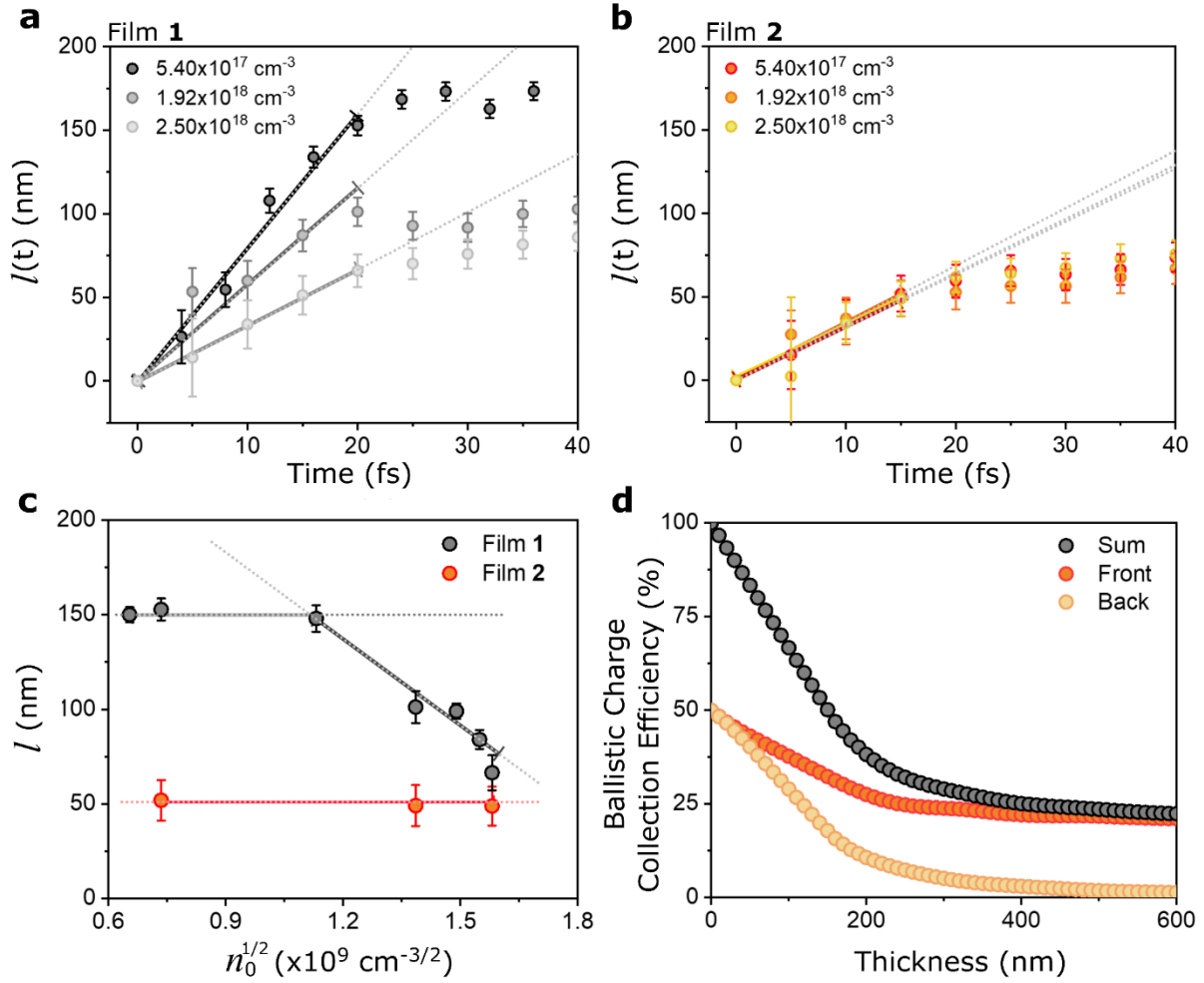


**Figure 4. Ballistic transport of non-equilibrium carriers.** **a**, Carrier density dependence on the transport length,  $l(t)$ , of film 1. **b**, Carrier density dependence on the transport length for film 2. The spatial evolutions of both film 1 and 2 were obtained at 720 nm upon excitation at 580 nm. The pump fluence was varied between 150 to 900 fJ. **c**, The ballistic transport length plotted as a function of the square root of carrier density to take account of the bimolecular nature of carrier-carrier scattering. The ballistic transport distance are obtained at 20 and 15 fs for film 1 and 2, respectively by using  $l(t) \approx \sqrt{\sigma^2(t) - \sigma^2(0)}$ , where  $\sigma(0)$  is the width of carrier distribution obtained at zero pump probe delay. **d**, The ballistic charge collection efficiency, defined as the fraction of non-equilibrium carriers reaching the charge transport layers ballistically, plotted as a function of the thickness of perovskite layer. The charge collection efficiency curves were obtained by assuming that the non-equilibrium carriers have the ballistic transport length of 150 nm. **Error bars represent standard deviation widths from the 2D Gaussian fit as discussed in detail in Supplementary Section 4.**